

1 **Simultaneous OI 630 nm imaging observations of thermospheric gravity waves and**
2 **associated revival of fossil depletions around midnight near the EIA crest**

3
4
5 **Authors:**

6 **1. Navin Parihar**

7 Indian Institute of Geomagnetism, Navi Mumbai, India

8 e-mail: navindeparihar@gmail.com

9
10 **2. Saranya Padincharapad**

11 (a) Equatorial Geophysical Research Laboratory, Indian Institute of Geomagnetism,
12 Tirunelveli, India

13 (b) Manonmaniam Sundaranar University, Tirunelveli, India

14 e-mail: anuja8494@gmail.com

15
16 **3. Anand Kumar Singh**

17 National Centre for Polar and Ocean Research, Goa, India

18 e-mail: singhaaks@gmail.com

19
20 **4. Prasanna Mahavarkar**

21 Indian Institute of Geomagnetism, Navi Mumbai, India

22 e-mail: mahavarkarprasanna@gmail.com

23
24
25 **Corresponding Author:**

26 **Navin Parihar**, Indian Institute of Geomagnetism, Navi Mumbai, India

27 e-mail: navindeparihar@gmail.com

28
29
30
31 **Key Words:**

32 Airglow imaging; Midnight Irregularities/Depletions; Gravity wave seeding; Low-
33 latitude ionosphere.

35 **Abstract**

36 We report the F-region airglow imaging of fossil plasma depletions around midnight that
37 revived afresh under the persisting thermospheric gravity wave (GW) activity. An all-sky
38 imager recorded these events in OI 630 nm imaging over Ranchi (23.3° N, 85.3° E, mlat. ~19°
39 N), India, on 16 April 2012. Northward propagating and east-west aligned GWs (λ ~210 km,
40 v ~64 m/s, and τ ~0.91 h) were seen around midnight. Persisting for ~2 hours, this GW
41 activity revived two co-existing and eastward drifting fossil depletions, DP1 and DP2. GWs-
42 driven revival was prominently seen in depletion DP1, wherein its apex height grew from
43 ~600 km to >800 km, and the level of intensity depletion increased from ~17% to 50%.
44 Present study is novel in the sense that simultaneous observations of thermospheric GWs
45 activity and associated evolution of depletion in OI 630 nm airglow imaging, and that too
46 around local midnight, have not been reported earlier. Current understanding is that GW
47 phase fronts aligned parallel to the geomagnetic field lines and eastward propagating are
48 more effective in seeding Rayleigh-Taylor (RT) instability. Here, GW fronts were east-west
49 aligned (i.e. perpendicular to the geomagnetic field lines) and propagated northward, yet they
50 revived fossil depletions.

51

52

53 1. Introduction

54 Gravity waves (GWs) are well-known to influence the mesosphere-lower thermosphere-
55 ionosphere (MLTI) region. GWs significantly contribute to the momentum and energy budget
56 of the MLT region via the wave-dissipation processes (Fritts and Alexander, 2003; Holton,
57 1983). Apart from the dominant solar and geomagnetic inputs, GWs are the key element in
58 some of the electrodynamic processes in the ionosphere e.g. irregularities, atmosphere-
59 ionosphere (AI) coupling, traveling ionospheric disturbances, etc.. In the equatorial F-region,
60 GWs modulate the ionospheric plasma into wave-like ionization structures. Under favourable
61 conditions, these structures act as a seed to Generalized Rayleigh-Taylor (GRT) instability
62 that generates the irregularities (Fritts et al., 2009; Huba and Joyce, 2007, 2010; Huba and
63 Liu, 2020; Hysell et al., 1990; Kelley, 2009; Woodman, 2009). GWs are also important in the
64 AI coupling during deep convection activity, thunderstorms, lightning, cyclones, tornadoes,
65 transient luminous events (TLEs)/sprites initiation, tsunamis, etc. (Azeem and Barlage, 2018;
66 Maurya et al., 2022; Huba et al., 2015). GWs can also generate medium-scale traveling
67 ionospheric disturbances (MSTIDs) (Fukushima et al., 2012; Figueiredo et al., 2018; Heale et
68 al., 2022, and references cited therein). On the course of their propagation, GWs can also
69 induce periodic fluctuations in the ionospheric parameters e.g. the electron density or total
70 electron content (TEC), the F-region height, temperatures and winds, etc. (Ford et al., 2006,
71 2008; Klausner et al., 2009; Parihar et al., 2018; Vadas and Azeem, 2021) or airglow
72 emission (Huba et al., 2015; Makela et al., 2011).

73

74 The crucial role of GWs in seeding the post-sunset equatorial spread-F (ESF) or plasma
75 bubbles (EPBs) is fairly well understood (Abdu et al., 2009; Fritts et al., 2009; Huba and
76 Joyce, 2007, 2010; Hysell et al., 1990; Kelley, 2009; Singh et al., 1997; Tsunoda, 2010;
77 Tulasi Ram et al., 2014; Woodman, 2009). However, their role in the seeding of the
78 midnight/post-midnight irregularities remains poorly understood, especially when the
79 important criteria for the triggering of the GRT instability are absent (e.g., the favorable
80 alignment of the solar terminator with the geomagnetic field lines and the pre-reversal
81 enhancement, PRE, of the zonal electric field). Lately, Huba and Liu (2020) reported the
82 global simulations of the ESF using the SAMI3/WACCM-X coupled model. SAMI3 is the
83 abbreviation for ‘*Sami3 is Another Model of Ionosphere*’ (Huba et al., 2008), and WACCM-
84 X stands for the ‘*Whole Atmosphere Community Climate Model with thermosphere and*
85 *ionosphere extension*’ (Liu et al., 2010). For the first time, Huba and Liu’s (2020) simulations
86 demonstrated that GWs are the dominant seed mechanism and can spontaneously generate

87 the ESF, and that the EPBs develop self-consistently in the postsunset ionosphere. Studies by
88 Nishioka et al. (2012) show that the GRT instability can occur near midnight under the
89 influence of enhanced GW activity and then can lead to the growth of irregularities. MSTIDs
90 are an important generation mechanism of post-midnight irregularities wherein the electric
91 field perturbations associated with them acts as the seed (Miller et al., 2009; Taori et al.,
92 2015). Otsuka (2018) have presented an elaborative review of these mechanisms. All-sky
93 airglow imaging (ASAI) along with the radar, ionosonde, and GPS measurements have
94 significantly contributed to our understanding of the crucial role of GWs in seeding the EPBs
95 (Mendillo and Baumgardner, 1982; Mendillo et al., 1997; Taori et al., 2010; Yadav et al.,
96 2017). *Spread-F Experiment (SpreadFEx)* carried out in Brazil during September-November
97 2005 is one such example (Fritts et al., 2009). In the Indian subcontinent, Sreeja et al. (2009)
98 reported the GWs in OI 630 nm dayglow intensity variations that acted as a seed to the ESF
99 irregularities.

100

101 GWs that give rise to the EPBs have usually been reported in the MLT region airglow
102 imaging (e.g. Fritts et al., 2009; Paulino et al., 2011; Takahashi et al., 2009; Taori et al.,
103 2013). Reports featuring them in the F-region airglow imaging are rare and limited to that of
104 Makela et al. (2011), Paulino et al. (2016, 2018), Sau et al. (2018), and Smith et al. (2015).
105 Makela et al. (2011) and Smith et al. (2015) reported the thermospheric imaging observations
106 of GWs associated with tsunami and earthquake, respectively. Paulino et al. (2016, 2018) and
107 Sau et al. (2018) presented their observations in OI 630 nm imaging from Brazil and India,
108 respectively. However, these authors did not report any occurrence of depletions during the
109 undergoing GW activity. We report, for the first time, simultaneous observations GWs and
110 depletions in the F-region airglow imaging.

111

112 On the course of temporary campaign-based ASAI observations of OI 630 nm emission
113 under *Climate And Weather of Sun-Earth System (CAWSES) India Phase II Programme*
114 at Ranchi (23.3° N, 85.3° E, mlat. ~19° N), GW activity and “fossil depletions” were seen
115 together on 16 April 2012 with the former reviving the latter. Fossil depletions are the
116 remnants of airglow depletion or EPBs that have ceased growing upward or poleward;
117 however, they continue to persist and move with ambient plasma drift. Under *Maui Middle*
118 *Atmosphere and Lower Thermosphere (Maui-MALT)* initiative, Makela et al. (2004) reported
119 their extensive observations in OI 630 nm imaging from Haleakala Volcano (20.7° N, 203.7°
120 E; mlat. 21.3° N), Hawaii during the solar maximum of 2002-2003. Chapagain et al. (2011)

121 presented their limited observations from Christmas Island (2.1° N, 157.4° W, mlat. 2.8° N)
122 during September 1995. In India, Sekar et al. (2007) presented their case study from Gadanki
123 (13.5° N, 79.2° E, mlat. 6.3° N). However, these investigations did not discuss any
124 resurgence of fossil depletions associated with the GW activity. Novelty of this study is that
125 the “fossil depletions” revived into “active depletions” after the emission layer witnessed the
126 GW activity. Lately, Wrasse et al. (2021) presented an interesting event wherein a fossil EPB
127 merged with other ones after interacting with an electrified MSTID and turned into an active
128 bubble.

129

130

131 **2. Instrumentation and data**

132 Under the *CAWSES India Phase II Programme*, an ASAI was installed for limited
133 nightglow observations at Ranchi (23.3° N, 85.3° E, mlat. $\sim 19^{\circ}$ N), located near the crest of
134 equatorial ionization anomaly (EIA) in India during April 2012. Parihar et al. (2017) and
135 Parihar (2019) have described this ASAI system in detail. OI 630 nm emission was
136 monitored using a 2.2 nm half-power bandwidth optical filter having transmittance of $\sim 77\%$.
137 Our imager’s field-of-view roughly covered about $7\text{-}8^{\circ}$ latitude/longitude region at 250 km
138 over Ranchi. Airglow images were flat-fielded to reduce the inhomogeneous contribution at
139 lower elevations due to van Rhijn effect and non-uniform sensitivity of CCD detector at
140 different pixels. Next, following the technique described by Wrasse et al. (2021), we
141 detrended the individual images to enhance the contrast of airglow features using an hour
142 running average image. Using known astral positions and assuming OI 630 nm emission peak
143 at 250 km, the geographic coordinates of each pixel was determined following the technique
144 of Garcia et al. (1997). Using this information, all-sky images were unwarped. We follow the
145 technique discussed by Pimenta et al. (2003) to determine the drift velocity of depletions.
146 First, for a given latitude, two intensity profiles along east-west direction as a function of
147 distance was generated using two successive unwarped images. Next, the east-west
148 displacement of depletion was estimated using these two profiles from which drift speed was
149 determined (see Pimenta et al., 2003 for details of this technique). Similarly, the propagation
150 characteristics of GW fronts were estimated by tracking faint crest and trough along the
151 propagation direction in the consecutive images. As GW fronts were unclear in images, we
152 used contrast-enhanced images. We, also, generated NS keograms to visualize GW traces and
153 determine their speed. A keogram is a time-versus-latitude plot generated by extracting a NS
154 column from individual images and stacking them horizontally. Next, GWs speed was, also,

155 estimated from the slope of wave traces seen in these keograms (Makela et al., 2006). We
156 looked into the total electron content (TEC) measurements from an *International GNSS*
157 *Service* station Hyderabad (17.3° N, 78.6° E, mlat. ~12.0° N, located nearby and south of
158 Ranchi) to ascertain GW activity seen in the ASAI observations (Source: [https://t-
159 ict4d.ictp.it/nequick2/gnss-tec-calibration](https://t-ict4d.ictp.it/nequick2/gnss-tec-calibration), Ciruolo et al., 2007). Quiet geomagnetic
160 conditions prevailed on this night with $Kp < 2$, $Ap = 4$, and $-4 < Dst < 10$ nT.

161
162

163 3. Observations

164 Such GWs-driven revival of “fossil depletions” was recorded in airglow images during 1700-
165 2000 UT on 16 April 2012. Here, Indian Standard Time (IST) = Universal Time (UT) + 0530
166 and Local Time (LT) \approx IST. As such, 1700-2000 UT corresponds to ~1.5 h duration before
167 and after the local midnight. Figures 1 and 2 present airglow images that depict this event
168 seen over Ranchi during 1742-1942 UT on 16 April 2012. As the faint airglow features were
169 getting lost in the unwarping process, warped all-sky images are presented. Supplementary
170 material S1 shows the movie created from these images that feature this event. Fossil
171 depletions of our interest that showed the GWs-driven revival are marked as **DP1** and **DP2** in
172 Figure 1 and 2. Here, **ROI1** is the region-of-interest wherein a few weakly perceivable fronts
173 of GWs and fossil depletions coexisted initially.

174

175 3.1 Signatures of GW activity in the F-region

176 We first observed faint signatures of GW activity near the southern edge of the field-of-view
177 (FOV) during ~1715-1724 UT. Successive images showed unclear signatures of GWs
178 activity. Starting ~1730 UT, their presence became more evident and continued until 1906
179 UT or so. GWs fronts were not clearly seen because of their interaction with co-existing
180 depletions. Some weakly perceivable bright fronts are marked as ‘f1’, ‘f2’, ‘f3’ and ‘f4’ in
181 Figure 1 and 2. Similarly, dark trough that precede fronts ‘f1’ and ‘f2’ are marked as ‘t1’ and
182 ‘t2’, respectively. Often GWs in OI 630 nm imaging are faint and unclear. Under similar
183 situations, Makela et al. (2011) found that time difference (TD) images have proven ability to
184 reflect such GWs faint fronts. In their work, initial analysis of raw images did not show any
185 GWs activity linked with tsunami; however, TD images indeed reflected associated GWs. We
186 generated such TD images and are shown in Figure 3 which clearly show dark troughs ‘t1’
187 and ‘t2’ and GW fronts ‘f1’ and ‘f2’. North-south (NS) keograms [shown in Figure 4 (a) and

188 (b)] showed a few clear alternating bright and dark intensity striations over the north, and
189 their slope indicates that GWs propagated towards the north. We estimated GWs propagation
190 characteristics using the slope of wave traces (marked by black arrow 'b1', 'b2', 'b3', 'b4') in
191 keograms and cross-verified them with the intensity profiling technique. We found that these
192 GWs propagated from the south to north with the phase speed (v) of $\sim 64 \pm 2$ m/s and had the
193 horizontal wavelength (λ) and period (τ) of $\sim 210 \pm 6$ km and $\sim 0.91 \pm 0.06$ h, respectively.

194

195 We further looked into the TEC measurements from IGS station Hyderabad (17.3° N, 78.6°
196 E, mlat. $\sim 12.0^\circ$ N), India to confirm this on-going GWs activity. Figure 5 shows the TEC
197 measurements depicting GW activity in and around Hyderabad during 1700-2000 UT on this
198 night. Figure 5 (a) shows the scatter plots of the TEC along the trajectory of ionospheric
199 pierce points (IPPs) for different GPS satellites during 1700-1930 UT on this night. PRN
200 numbers of GPS satellites, along with the start time at 1700 UT, are indicated next to the
201 corresponding IPPs trajectory. TEC variations along the NS-aligned IPPs tracks (e.g. G27
202 and G28) clearly show the wavelike fluctuations in the 15 - 20° N latitude range. The temporal
203 evolution of the TEC for a few satellites is shown in Figure 5 (b). Of our interest is G28's
204 TEC measurement as its IPPs trajectory lay close to the imager's ROI1 during 1700-1800 UT
205 which showed a strong signature of GWs. By performing the periodogram analysis of the
206 temporal and spatial variation of its TEC, we estimated the propagation characteristics of GW
207 to be $\tau \sim 0.95 \pm 0.03$ h, $\lambda \sim 229 \pm 12$ km, and $v \sim 67 \pm 5$ m/s, and is in good agreement with the
208 ASAI observations. Further, the propagation direction of GWs seen in airglow imaging is in
209 good agreement with these previous reports. Studies on the GW activity at the MLT heights
210 over a farther low-latitude station Prayagraj (25.5° N, formerly Allahabad) in India showed
211 their propagation either northward or northeast around midnight during April-May
212 (Mukherjee et al., 2010). A comprehensive study of thermospheric GWs in the ASAI
213 observations over Tirunelveli (8.7° N) in India during 2013-2015 indicated their propagation
214 toward the north-northwest during the equinoxes (Sau et al., 2018).

215

216 **3.2 GWs-driven revival of fossil depletions**

217 During 1730-1748 UT, faint signatures of depletion DP1 that revived were seen in the ROI1.
218 Depletion DP1 lacked any poleward growth during 1730-1806 UT. Using the equation given
219 in Kelley (2009) and by tracking the poleward tip of depletion, we estimated the apex height
220 of the associated geomagnetic flux tubes (A_H) and found it to be steady at ~ 600 km. Within it,

221 the level of intensity reduction with respect to that of the ambient region (i.e., $\Delta I/I_{\text{ambient region}}$)
222 was $\sim 17\%$. However, depletion DP1 drifted gradually to the east with a speed of 59-70 m/s.
223 Beginning 1812-1818 UT, this depletion started to intensify steadily, gain contrast against the
224 background and become noticeable. Southern end of depletion DP1 was fused with that of a
225 preceding depletion OD2. A few faint NS-aligned depletions were also present in the ROI1.
226 Along with depletion DP1, they intersected the EW-aligned fronts 'f1' and 'f2' of GWs, and
227 fragmented them into few isolated structures. Later on, these structures got attached to the
228 west wall of depletion DP1 and started moving in unison. Clear signs of two such fragments
229 (marked as S1 and S2 in Figure 1 and 2) can be seen at ~ 1830 UT and ~ 1806 -1812 UT,
230 respectively. Starting 1824-1830 UT, we noted airglow enhancement to occur near its east
231 wall that then started to become distinct. As a result, an *inverted arrowhead*-shaped depletion
232 with an unusually wide southern fraction was evident during 1836-1854 UT. As two attached
233 structures S1 and S2 drifted along with depletion DP1, they tilted considerably to the east by
234 ~ 60 - 75° (see the ASAI images beginning 1830 UT in Figures 1 and 2). At ~ 1900 UT, the
235 structure S1 was almost aligned and merged with the west wall of depletion DP1, which led
236 to a fairly distinct west wall (seen as weak airglow enhancement). Airglow enhancement near
237 both the east and west wall (marked as A1 and A2, respectively, in Figure 2) continued, and a
238 linear NS-aligned depletion DP1 (having $A_H > 800$ km and $\Delta I/I_{\text{ambient region}} \sim 50\%$) was seen at
239 1906-1912 UT. Within the next 6-12 min, the apex of structure S2 merged with airglow
240 enhancement A2 near the west wall.

241

242 Next, some airglow enhancement occurred in the inner edge of the west wall of depletion
243 DP1 at 1924 UT (see the region-of-interest, ROI2 in Figure 2). We interpret this as a
244 consequence of some ambient plasma intrusion across its west wall. Later, such intrusion led
245 to the disappearance of its southern fraction and the formation of an isolated depletion at
246 1942 UT. Possibly these disappearances occurred due to the filling of the EIA plasma into
247 depletion across its western wall (see Otsuka et al., 2012). Similarly, fossil depletion DP2
248 also revived; however, its evolution was much simpler than that of depletion DP1.

249

250 **4 Discussions**

251 We present rare simultaneous observations of GWs activity and associated revival of fossil
252 depletions in the F-region airglow imaging around midnight over an off-equatorial station
253 Ranchi (located near the EIA crest) in India. Post-sunset ionospheric irregularities, in the

254 equatorial region, are generated by the GRT instability that sets off under the suitable
255 combination of (i) favourable alignment of solar terminator with geomagnetic field lines; (ii)
256 rapid height rise of the F-layer; (iii) absence of strong transequatorial wind and (iv) necessary
257 seed perturbation (Fejer and Kelley, 1980; Kelley, 2009; Makela and Otsuka, 2012;
258 Woodman, 2009). Stronger the height rise of the F-layer and an initial seed perturbation is,
259 the faster the growth rate of GRT instability, which ultimately leads to the rapid evolution of
260 the irregularities (Huba and Joyce, 2007; Huang et al., 1993; Hysell et al., 2014; Kelley et al.,
261 1981; Krall et al., 2013; Tsunoda, 2010; Zalesak and Ossakow, 1980). **GWs are well known**
262 **to deform the bottom side plasma of the F-region into the wavelike ionization structures that**
263 **then act as a seed to GRT instability, which, in turn, generates irregularities (Kelley et al.,**
264 **1981; Hysell et al., 1990; Huba and Liu, 2020).** While their role in the generation of the post-
265 sunset irregularities is well known, our understanding is limited in the context of
266 midnight/post-midnight irregularities. Present study features midnight fossil airglow
267 depletions that revived due to undergoing GW activity and turned into an active depletion.

268

269 Northward propagating GWs having $\lambda \sim 210$ km, $v \sim 64$ m/s, and $\tau \sim 0.91$ h were recorded in
270 630 nm nightglow images during 1715-1906 UT. Supporting airglow observations, TEC
271 measurements, too, showed the presence of similar GWs. Simultaneously, an eastward
272 drifting fossil depletion DP1 ($A_H \sim 600$ km and $\Delta I/I_{\text{ambient region}} \sim 17\%$) co-existed during
273 1730-1748 UT. Next, depletion DP1 and other co-existing depletions intercepted EW-aligned
274 GW fronts and fragmented them during 1806-1824 UT. Subsequently, two such fragments
275 viz. S1 and S2 that lay close to depletion DP1 got attached to its west wall, started drifting
276 eastward in unison, tilted significantly to the east, and almost got aligned with the west wall.
277 Next, depletion DP1 gradually intensified, surged polewards, and became a well-developed
278 linear depletion ($A_H > 800$ km and $\Delta I/I_{\text{ambient region}} \sim 50\%$) during 1906-1912 UT. Meanwhile,
279 airglow enhancement continued to develop near both its walls and an uneven broadening was
280 seen in its southern half. Next, some ambient plasma diffusion occurred near this uneven
281 region leading to airglow enhancement in the inner edge of its west wall at 1924 UT. Such
282 intrusion continued, its southern fraction gradually disappeared, and an isolated depletion was
283 formed at 1942 UT. Present observations clearly indicate that “fossil depletion” DP1 revived
284 and became an “active depletion” under the influence of co-existing GWs activity. Another
285 succeeding depletion, DP2, too, showed a similar revival.

286

287 An important consideration in the GWs seeding of the GRT instability is the alignment of
288 their wavefronts with the geomagnetic field lines. The current understanding is that the
289 strength of the polarization electric field generated by the GWs greatly depends on the angle
290 between them, and the maximum polarization occurs when their wavefront is aligned with the
291 geomagnetic field (Huba et al., 2015; Hysell et al., 2014; Krall et al., 2013; Tulasi Ram et al.,
292 2014; Tsunoda, 2010). Numerical simulations by Hysell et al. (2014) suggest that the GWs-
293 induced modulations were the most severe when their fronts were aligned with the magnetic
294 meridian. Using Communications/Navigation Outage Forecasting System (C/NOFS) mission
295 TEC measurements, Tulasi Ram et al. (2014) studied the characteristics of large-scale wave
296 structure (LSWS) at the base of the F-region and their association with the EPBs occurrences
297 in Southeast Asia and Africa. Authors found that the EPBs frequently occurred when the
298 amplitudes of LSWS were adequately increased, and their phase fronts were geomagnetic
299 field-aligned.

300

301 In the present study, the GWs fronts were east-west aligned (i.e., transverse to the
302 geomagnetic field lines) and propagated northward. Yet, fossil depletions DP1 and DP2
303 revived and is intriguing. Meridional wind perturbations associated with GWs are known to
304 be ineffective in the initiation and development of depletions. Present observations are in
305 contrast with this notion and point towards another excitation mechanism rather than GRT
306 instability, which we conjecture, is the spatial resonance mechanism for these reasons. Good
307 matching was seen between the GWs phase speed ($v \sim 64\text{-}67$ m/s) and the eastward drift of
308 depletion DP1 ($v \sim 59\text{-}70$ m/s). Horizontal Wind Model 2007 estimates also indicated the
309 zonal thermospheric wind speed of 51-61 m/s (Drob et al., 2008). We estimated the speed at
310 which the apex of DP1 progressed poleward and found it to be in the range of 46-56 m/s.
311 Spatial resonance theory of GWs seeding of irregularities states that the effects of GWs
312 perturbations are the strongest when its phase speed and the plasma drift velocity are nearly
313 equal (Kelley et al., 1981). Under such conditions, the ionospheric plasma exerts the GW-
314 associated forcing for a longer duration; thereby, accelerating the formation of ionization
315 structures. As such, we conjecture that this GWs-driven revival of fossil depletions occurred
316 via the spatial resonance mechanism. Numerical simulations by Huang and Kelley (1996)
317 suggest that this mechanism can accelerate the formation of depletions. Possibly continuously
318 undergoing GWs activity for 2 hours in the F-region sufficiently intensified the magnitude of

319 associated ionization modulations, which in turn triggered and sustained the revival of fossil
320 depletions via the spatially resonant mechanism.

321

322 Meridional wind can influence the growth rate of GRT instability by altering the field-line
323 integrated Pederson conductivity. Maruyama (1988) and Abdu et al. (2006) found that strong
324 meridional winds could reduce the growth rate of RTI and suppress irregularities. Huba and
325 Krall (2013) have reported both stabilizing and destabilizing effects of the meridional winds
326 on RT instability. Devasia et al. (2002) found that a suitable combination of the meridional
327 wind and F-region base height favours ESF development. In the present study, the meridional
328 wind measurements using a Fabry-Perot interferometer, etc. were not available; hence, their
329 possible role in the evolution of these fossil depletions could not be investigated.

330

331 We know that the electric field perturbations associated with MSTIDs can influence the
332 growth of irregularities. Otsuka et al. (2012) and Shiokawa et al. (2015) reported the
333 disappearance of an EPB upon interaction with MSTIDs and large-scale traveling ionospheric
334 disturbances (LSTIDs), respectively. Authors suggested that the electric field associated with
335 MSTIDs/LSTIDs can move ambient plasma into the bubble across the geomagnetic field line
336 through $\mathbf{E} \times \mathbf{B}$ drift which will result in the filling and subsequent disappearance of the
337 depletion. Studies by Miller et al. (2009), Taori et al. (2015) and Takahashi et al. (2020)
338 suggest that MSTIDs can directly seed EPBs. Simulation studies by Krall et al. (2011),
339 further, indicates that the electric field associated with electrified MSTIDs can enhance the
340 growth of EPBs. Lately, Wrasse et al. (2021) presented an interesting observations of the
341 interaction of a fossil EPB with an electrified MSTID over 13.3° S. After interaction with the
342 MSTID, concerned fossil EPB merged with other four EPBs, developed poleward and
343 bifurcated. Using detrended TEC data, Takahashi et al. (2021) studied the LSWS over Latin
344 America and found them to be effective in seeding EPBs.

345

346 **5 Summary**

347 We present, here, airglow imaging observations of fossil plasma depletions that revived
348 afresh under the action of prolonged GW activity and became active depletions. Such
349 simultaneous imaging of thermospheric GWs and depletions was recorded in the ASAI of OI
350 630 nm emission over Ranchi (mlat. ~19° N), India, on 16 April 2012. Salient features of the
351 present study are as under:

- 352 1. First, airglow images showed EW-aligned and SN-propagating GWs ($\lambda \sim 210$ km, v
353 ~ 64 m/s, and $\tau \sim 0.91$ h) over Ranchi during 1715-1906 UT. Similar GWs were, also,
354 seen in TEC measurements over a lower latitude station Hyderabad.
- 355 2. A co-existing and prominent fossil depletion DP1 revived under this GW activity
356 wherein its apex raised from 600 km to >800 km, and the level of intensity depletion
357 increased from 17 % to 50 %. Another fossil depletion DP2, too, revived.
358 Interestingly, GWs phase fronts were transverse to the geomagnetic field lines, yet
359 two fossil depletions revived under their influence and became active depletions.
- 360 3. As GWs phase speed ($v \sim 64-67$ m/s) nearly matched the eastward drift of depletion
361 DP1 ($v \sim 59-70$ m/s), we conjecture that the GWs-driven revival of these fossil
362 depletions possibly occurred via the spatial resonance mechanism.
- 363 4. An uneven region of increased thickness existed on the southern half of the revived
364 depletion DP1, wherein some airglow enhancement was seen later in the inner edge of
365 its west wall. Possibly the gradual disappearance of its southern fraction occurred
366 because of the intrusion of ambient plasma across the west wall.

367

368 Contrary to the current understanding, this study shows that the GWs fronts aligned
369 perpendicular to the geomagnetic field lines can effectively grow irregularities. Present
370 observations of the GWs-driven revival of fossil airglow depletions further contribute to our
371 understanding of their generation mechanism around midnight.

372

373

374 **Data Availability.** Airglow data used in the present study are available through the
375 institutional data repository (<http://www.iigm.res.in/>) or
376 <https://doi.org/10.5281/zenodo.8143215>. Movie created from all-sky 630 nm nightglow
377 images showing the gravity wave activity and the evolution of depletion DP1 and DP2 is
378 available from <https://doi.org/10.5281/zenodo.8358134>. Calibrated TEC data is available
379 from <https://t-ict4d.ictp.it/nequick2/gnss-tec-calibration>.

380

381

382 **Author contributions.** NP conceptualized the research problem and prepared the first draft.
383 All authors contributed to the interpretation of results, discussion, and subsequent drafting of
384 the manuscript.

385
386
387
388
389
390
391
392
393
394
395
396
397
398
399
400
401
402
403
404
405
406
407
408
409
410
411
412
413
414
415
416
417
418

Acknowledgements: Funds for Airglow Research at *Indian Institute of Geomagnetism* are being provided by *Department of Science and Technology (DST), Govt. of India, New Delhi*. GNSS TEC Calibrated data were downloaded from <https://t-ict4d.ictp.it/nequick2/gnss-tec-calibration> and *Telecommunications/ICT for Development (T/ICT4D) Laboratory of the Abdus Salam International Centre for Theoretical Physics, Trieste, Italy* is gratefully acknowledged. *SP* is grateful to *Director, Indian Institute of Geomagnetism, Navi Mumbai* for the award of Research Scholarship. **Authors sincerely thank the Editor and Reviewers for their encouragement and critical comments.**

References:

Abdu, M., Iyer, K. N., de Medeiros, R., Batista, I. S. and Sobral, J. H.: Thermospheric meridional wind control of equatorial spread F and evening prereversal electric field, *Geophys. Res. Lett.* 33 (7). <http://dx.doi.org/10.1029/2005GL024835>, 2006.

Abdu, M. A., Kherani, E. A., Batista, I. S., de Paula, E. R., Fritts, D. C., and Sobral, J. H.: Gravity wave initiation of equatorial spread F/plasma bubble irregularities based on observational data from the SpreadFEx campaign, *Ann. Geophys.*, 27, 2607-2622. <https://doi.org/10.5194/angeo-27-2607-2009>, 2009.

Azeem, I., and Barlage, M.: Atmosphere-ionosphere coupling from convectively generated gravity waves. *Adv. Space Res.*, 61(7), 1931-1941. <https://doi.org/10.1016/j.asr.2017.09.029>, 2018.

Ciraolo, L., Azpilicueta, F., Brunini, C., Meza, A. and Radicella, S. M.: Calibration errors on experimental slant total electron content (TEC) determined with GPS. *J. Geod.*, 81, 111–120, <https://doi.org/10.1007/s00190-006-0093-1>, 2007.

Chapagain, N. P., Taylor, M. J., and Eccles, J. V.: Airglow observations and modeling of F region depletion zonal velocities over Christmas Island, *J. Geophys. Res.*, 116, A02301, <https://doi.org/10.1029/2010JA015958>, 2011.

419 Devasia, C., Jyoti, N., Subbarao, K., Viswanathan, K., Tiwari, D. and Sridharan, R.: On the
420 plausible linkage of thermospheric meridional winds with the equatorial spread F, *J. Atmos.*
421 *Sol.-Terrest. Phys.* 64 (1), 1–12, [http://dx.doi.org/10.1016/S1364-6826\(01\)00089-X](http://dx.doi.org/10.1016/S1364-6826(01)00089-X), 2002.
422

423 Drob, D. P., Emmert, J. T., Crowley, G., Picone, J. M., Shepherd, G. G., Skinner, W., et al.:
424 An empirical model of the Earth's horizontal wind fields: HWM07. *J. Geophys. Res.*, 113,
425 A12304, <https://doi.org/10.1029/2008JA013668>, 2008.
426

427 Fejer, B. G., and Kelley, M. C.: Ionospheric irregularities. *Rev. Geophys.*, 18(2), 401-454,
428 <https://doi.org/10.1029/RG018i002p00401>, 1980.
429

430 Figueiredo, C. A. O. B., Takahashi, H., Wrasse, C. M., Otsuka, Y., Shiokawa, K., & Barros,
431 D.: Medium-scale traveling ionospheric disturbances observed by detrended total electron
432 content maps over Brazil. *Journal of Geophysical Research: Space Physics*, 123, 2215–2227.
433 <https://doi.org/10.1002/2017JA025021>, 2018.
434

435 Ford, E. A. K., Aruliah, A. L., Griffin, E. M., and McWhirter, I.: Thermospheric gravity
436 waves in Fabry-Perot Interferometer measurements of the 630.0nm OI line, *Ann. Geophys.*,
437 24, 555–566, <https://doi.org/10.5194/angeo-24-555-2006>, 2006.
438

439 Ford, E. A. K., Aruliah, A. L., Griffin, E. M., and McWhirter, I.: Statistical analysis of
440 thermospheric gravity waves from Fabry-Perot Interferometer measurements of atomic
441 oxygen, *Ann. Geophys.*, 26, 29–45, <https://doi.org/10.5194/angeo-26-29-2008>, 2008.
442

443 Fritts, D. C., and Alexander, M. J.: Gravity wave dynamics and effects in the middle
444 atmosphere, *Rev. Geophys.*, 41, 1003, <https://doi.org/10.1029/2001RG000106>, 1, 2003.
445

446 Fritts, D. C., Abdu, M. A., Batista, B. R., Batista, I. S., Batista, P. P., Buriti, R., Clemesha, B.
447 R., Dautermann, T., de Paula, E. R., Fechine, B. J., Fejer, B. G., Gobbi, D., Haase, J.,
448 Kamalabadi, F., Kherani, E. A., Laughman, B., Lima, P. P., Liu, H.-L., Medeiros, A., Pautet,
449 P.-D., Riggan, D. M., Rodrigues, F. S., São Sabbas, F., Sobral, J. H. A., Stamus, P.,
450 Takahashi, H., Taylor, M. J., Vadas, S. L., Vargas, F., and Wrasse, C. M.: Overview and
451 summary of the Spread F Experiment (SpreadFEx), *Ann. Geophys.*, 27, 2141–2155,
452 <https://doi.org/10.5194/angeo-27-2141-2009>, 2009.

453

454 Fukushima, D., Shiokawa, K., Otsuka, Y., and Ogawa, T.: Observation of equatorial
455 nighttime medium-scale traveling ionospheric disturbances in 630-nm airglow images over 7
456 years. *J. Geophys. Res.*, 117, A10324. <https://doi.org/10.1029/2012JA017758>, 2012.

457

458 Garcia, F. J., Taylor, M. J., and Kelley, M. C.: Two-dimensional spectra analysis of
459 mesospheric airglow image data. *Appl. Opt.*, 36(29), 7374-7385.
460 <https://doi.org/10.1364/AO.36.007374>, 1997.

461

462 Heale, C. J., Inchin, P. A., and Snively, J. B.: Primary versus secondary gravity wave
463 responses at F-region heights generated by a convective source, *J. Geophys. Res. Space*
464 *Physics*, 127, e2021JA029947, <https://doi.org/10.1029/2021JA029947>, 2022.

465

466 Huang, C.-S., Kelley, M. C., and Hysell, D. L.: Nonlinear Rayleigh-Taylor instabilities,
467 atmospheric gravity waves and equatorial spread F, *J. Geophys. Res.*, 98(A9), 15631-15642,
468 <https://doi.org/10.1029/93JA00762>, 1993.

469

470 Huang, C.-S., and Kelley, M. C.: Nonlinear evolution of equatorial spread F: 1. On the role of
471 plasma instabilities and spatial resonance associated with gravity wave seeding, *J. Geophys.*
472 *Res.*, 101(A1), 283-292, <https://doi.org/10.1029/95JA02211>, 1996.

473

474 Huba, J. D., and Joyce, G.: Equatorial spread F modeling: Multiple bifurcated structures,
475 secondary instabilities, large density ‘bite-outs’ and supersonic flows. *Geophys. Res. Lett.*,
476 34, L07105. <https://doi.org/10.1029/2006GL028519>, 2007.

477

478 Huba, J. D., Joyce, G., and Krall, J.: Three-dimensional equatorial spread F modeling,
479 *Geophys. Res. Lett.*, 35, L10102. <https://doi.org/10.1029/2008GL033509>, 2008.

480

481 Huba, J. D., and Joyce, G.: Global modeling of equatorial plasma bubbles, *Geophys. Res.*
482 *Lett.*, 37, L17104, <https://doi.org/10.1029/2010GL044281>, 2010.

483

484 Huba, J. D., and Krall, J.: Impact of meridional winds on equatorial spread F: Revisited,
485 *Geophys. Res. Lett.*, 40, 1268– 1272, doi:10.1002/grl.50292, 2013.

486

487 Huba, J. D., Drob, D. P., Wu, T.-W., and Makela, J. J.: Modeling the ionospheric impact of
488 tsunami-driven gravity waves with SAMI3: Conjugate effects. *Geophys. Res. Lett.*, 42,
489 5719–5726. <https://doi.org/10.1002/2015GL064871>, 2015.

490

491 Huba, J. D., and Liu, H.-L.: Global modeling of equatorial spread F with SAMI3/WACCM-
492 X. *Geophys. Res. Lett.*, 47, e2020GL088258. <https://doi.org/10.1029/2020GL088258>, 2020.

493

494 Hysell, D. L., Kelley, M. C., Swartz, W. E., and Woodman, R. F.: Seeding and layering of
495 equatorial spread F by gravity waves. *J. Geophys. Res.*, 95(A10), 17,253-17,260.
496 <https://doi.org/10.1029/JA095iA10p17253>, 1990.

497

498 Hysell, D. L., Jafari, R., Fritts, D. C., and Laughman, B.: Gravity wave effects on postsunset
499 equatorial F region stability, *J. Geophys. Res. Space Physics*, 119, 5847– 5860,
500 doi:10.1002/2014JA019990, 2014.

501

502 Kelley, M. C., Larsen, M. F., LaHoz, C., and McClure, J. P.: Gravity wave initiation of
503 equatorial spread F: A case study, *J. Geophys. Res.*, 86 (A11), 9087-9100,
504 <https://doi.org/10.1029/JA086iA11p09087>, 1981.

505

506 Kelley, M. C.: *The Earth's ionosphere: Plasma physics and electrodynamics* (2nd ed.).
507 Burlington, MA: Elsevier, 2009.

508

509 Klausner, V., Fagundes, P. R., Sahai, Y., Wrasse, C. M., Pillat, V. G., and Becker-Guedes, F.:
510 Observations of GW/TID oscillations in the F2 layer at low latitude during high and low solar
511 activity, geomagnetic quiet and disturbed periods, *J. Geophys. Res.*, 114, A02313,
512 <https://doi.org/10.1029/2008JA013448>, 2009.

513

514 Krall, J., Huba, J. D., Ossakow, S. L., Joyce, G., Makela, J. J., Miller, E. S., and Kelley, M.
515 C.: Modeling of equatorial plasma bubbles triggered by non-equatorial traveling ionospheric
516 disturbances. *Geophys. Res. Lett.*, 38(8), L08103. <https://doi.org/10.1029/2011GL046890>,
517 2011.

518

519 Krall, J., Huba, J. D., and Fritts, D. C.: On the seeding of equatorial spread F by gravity
520 waves, *Geophys. Res. Lett.*, 40, 661-664, <https://doi.org/10.1002/grl.50144>, 2013.

521
522 Makela, J. J., Ledvina, B. M., Kelley, M. C. and. Kintner, P. M: Analysis of the seasonal
523 variations of equatorial plasma bubble occurrence observed from Haleakala, Hawaii, *Ann.*
524 *Geophys.*, 22, 3109-3121, <https://doi.org/10.5194/angeo-22-3109-2004>, 2004.
525
526 Makela, J. J., Kelley, M. C., and Nicolls, M. J.: Optical observations of the development of
527 secondary instabilities on the eastern wall of an equatorial plasma bubble. *J. Geophys. Res.*,
528 111, A09311, <https://doi.org/10.1029/2006JA011646>, 2006.
529
530 Makela, J. J., Lognonne, P., Hebert, H., Gehrels, T., Rolland, L., Allgeyer, S., et al.: Imaging
531 and modeling the ionospheric airglow response over Hawaii to the tsunami generated by the
532 Tohoku earthquake of 11 March 2011. *Geophys. Res. Lett.*, 38, L00G02.
533 <https://doi.org/10.1029/2011GL047860>, 2011.
534
535 Makela, J. J., and Otsuka, Y.: Overview of nighttime ionospheric instabilities at low- and
536 mid-latitudes: Coupling aspects resulting in structuring at the mesoscale. *Space Sci. Rev.*,
537 168(1-4), 419-440. <https://doi.org/10.1007/s11214-011-9816-6>, 2012.
538
539 Maruyama, T.: A diagnostic model for equatorial spread F: 1. Model description and
540 application to electric field and neutral wind effects, *J. Geophys. Res.*, 93 (A12), 14611–
541 14622. <http://dx.doi.org/10.1029/JA093iA12p14611>, 1988.
542
543 Maurya, A. K., Parihar, N., Dube, A., Singh, R., Kumar, S., Chanrion, O., Tomicic, M., and
544 Neubert, T.: Rare observations of sprites and gravity waves supporting D, E, F-regions
545 ionospheric coupling, *Sci. Rep.*, 12, 581. <https://doi.org/10.1038/s41598-021-03808-5>, 2022.
546
547 Mendillo, M., and Baumgardner, J.: Airglow characteristics of equatorial plasma depletions.
548 *J. Geophys. Res.*, 87, 7641-7652, <https://doi.org/10.1029/JA087iA09p07641>, 1982.
549
550 Mendillo, M., Baumgardner, J., Colerico, M., and Nottingham, D.: Imaging science
551 contributions to equatorial aeronomy: initial results from the MISETA program, *J. Atmos.*
552 *Terr. Phys.*, 59, 1587-1599, [https://doi.org/10.1016/S1364-6826\(96\)00158-7](https://doi.org/10.1016/S1364-6826(96)00158-7), 1997.
553

554 Miller, E. S., Makela, J. J., and Kelley, M. C.: Seeding of equatorial plasma depletions by
555 polarization electric fields from middle latitudes: Experimental evidence, *Geophys. Res.*
556 *Let.*, 36, L18105, <https://doi.org/10.1029/2009GL039695>, 2009.

557

558 Mukherjee, G. K., Pragati Shikha, R., Parihar, N., Ghodpage, R. and Patil, P. T.: Studies of
559 the wind filtering effect of gravity waves observed at Allahabad (25.45° N, 81.85° E). *Earth*
560 *Planets Space* 62, 309-318, <https://doi.org/10.5047/eps.2009.11.008>, 2010.

561

562 Nishioka, M., Otsuka, Y., Shiokawa, K., Tsugawa, T., Effendy, , Supnithi, P., Nagatsuma, T.,
563 and Murata, K. T.: On post-midnight field-aligned irregularities observed with a 30.8-MHz
564 radar at a low latitude: Comparison with F-layer altitude near the geomagnetic equator, *J.*
565 *Geophys. Res.*, 117, A08337, <https://doi.org/10.1029/2012JA017692>, 2012.

566

567 Otsuka, Y., Shiokawa, K. and Ogawa, T.: Disappearance of equatorial plasma bubble after
568 interaction with mid-latitude medium-scale traveling ionospheric disturbance, *Geophysical*
569 *Research Letters*, 39, L14105, <https://doi.org/10.1029/2012GL052286>, 2012.

570

571 Otsuka, Y.: Review of the generation mechanisms of post-midnight irregularities in the
572 equatorial and low-latitude ionosphere. *Prog.. Earth Planet. Sci.* 5, 57.
573 <https://doi.org/10.1186/s40645-018-0212-7>, 2018.

574

575 Parihar, N., Singh, D., and Gurubaran, S.: A comparison of ground-based hydroxyl airglow
576 temperatures with SABER/TIMED measurements over 23° N, India, *Ann. Geophys.*, 35,
577 353–363, <https://doi.org/10.5194/angeo-35-353-2017>, 2017.

578

579 Parihar, N., Radicella, S. M., Nava, B., Migoya-Orue, Y. O., Tiwari, P., and Singh, R.: An
580 investigation of the ionospheric F region near the EIA crest in India using OI 777.4 and 630.0
581 nm nightglow observations. *Ann. Geophys.*, 36(3), 809-823. [https://doi.org/10.5194/angeo-](https://doi.org/10.5194/angeo-36-809-2018)
582 [36-809-2018](https://doi.org/10.5194/angeo-36-809-2018), 2018.

583

584 Parihar, N.: Rare occurrence of off-equatorial edge initiating and equatorward surging plasma
585 depletions observed in OI 630-nm imaging. *J. Geophys. Res. Space Physics*, 124, 2887-2896.
586 <https://doi.org/10.1029/2018JA026155>, 2019.

587

588 Paulino, I., Takahashi, H., Medeiros, A. F., Wrasse, C. M., Buriti, R. A., Sobral, J. H. A., and
589 Gobbi, D.: Mesospheric gravity waves and ionospheric plasma bubbles observed during the
590 COPEX campaign. *J. Atmos. Sol.-Terr. Phys.*, 73(11-12), 1575-1580.
591 <https://doi.org/10.1016/j.jastp.2010.12.004>, 2011.
592

593 Paulino, I., Medeiros, A. F., Vadas, S. L., Wrasse, C. M., Takahashi, H., Buriti, R. A., Leite,
594 D., Filgueira, S., Bageston, J. V., Sobral, J. H. A., and Gobbi, D.: Periodic waves in the lower
595 thermosphere observed by OI630 nm airglow images, *Ann. Geophys.*, 34, 293-301,
596 <https://doi.org/10.5194/angeo-34-293-2016>, 2016.
597

598 Paulino, I., Moraes, J. F., Maranhão, G. L., Wrasse, C. M., Buriti, R. A., Medeiros, A. F.,
599 Paulino, A. R., Takahashi, H., Makela, J. J., Meriwether, J. W., and Campos, J. A. V.:
600 Intrinsic parameters of periodic waves observed in the OI6300 airglow layer over the
601 Brazilian equatorial region, *Ann. Geophys.*, 36, 265–273, [https://doi.org/10.5194/angeo-36-](https://doi.org/10.5194/angeo-36-265-2018)
602 [265-2018](https://doi.org/10.5194/angeo-36-265-2018), 2018.
603

604 Pimenta, A. A., Fagundes, P. R., Sahai, Y., Bittencourt, J. A., and Abalde, J. R.: Equatorial F-
605 region plasma depletion drifts: latitudinal and seasonal variations. *Ann. Geophys.*, 21, 2315-
606 2322, <https://doi.org/10.5194/angeo-21-2315-2003>, 2003.
607

608 Sau, S., Narayanan, V. L., Gurubaran, S., and Emperumal, K.: Study of wave signatures
609 observed in thermospheric airglow imaging over the dip equatorial region. *Adv. Space Res.*,
610 62(7), 1762–1774, <https://doi.org/10.1016/j.asr.2018.06.039>, 2018.
611

612 Sekar, R., Chakrabarty, D., Sarkhel, S., Patra, A. K., Devasia, C. V., and Kelley, M. C.:
613 Identification of active fossil bubbles based on coordinated VHF radar and airglow
614 measurements, *Ann. Geophys.*, 25, 2099-2102, <https://doi.org/10.5194/angeo-25-2099-2007>,
615 2007.
616

617 Shiokawa, K., Otsuka, Y., Lynn, K. J., Wilkinson, P., and Tsugawa, T.: Airglow-imaging
618 observation of plasma bubble disappearance at geomagnetically conjugate points. *Earth*
619 *Planets and Space*, 67(1), 43, <https://doi.org/10.1186/s40623-015-0202-6>, 2015.
620

621 Singh, S., Johnson, F. S., and Power, R. A.: Gravity wave seeding of equatorial plasma
622 bubbles. *J. Geophys. Res.*, 102(A4), 7399–7410, <https://doi.org/10.1029/96JA03998>, 1997.
623

624 Smith, S. M., Martinis, C. R., Baumgardner, J., and Mendillo, M.: All-sky imaging of
625 transglobal thermospheric gravity waves generated by the March 2011 Tohoku Earthquake, *J.*
626 *Geophys. Res. Space Physics*, 120, 10,992-10,999, <https://doi.org/10.1002/2015JA021638>,
627 2015.
628

629 Sreeja, V., Vineeth, C., Pant, T. K., Ravindran, S. and Sridharan, R.: Role of gravity wavelike
630 seed perturbations on the triggering of ESF-First results from unique dayglow observations,
631 *Ann. Geophys.*, 27, 313-318, <https://doi.org/10.5194/angeo-27-313-2009>, 2009.
632

633 Takahashi, H., Taylor, M. J., Pautet, P.-D., Medeiros, A. F., Gobbi, D., Wrasse, C. M.,
634 Fechine, J., Abdu, M. A., Batista, I. S., Paula, E., Sobral, J. H. A., Arruda, D., Vadas, S. L.,
635 Sabbas, F. S., and Fritts, D. C.: Simultaneous observation of ionospheric plasma bubbles and
636 mesospheric gravity waves during the SpreadFEx Campaign, *Ann. Geophys.*, 27, 1477-1487,
637 <https://doi.org/10.5194/angeo-27-1477-2009>, 2009.
638

639 Takahashi, H., Wrasse, C. M., Figueiredo, C. A. O. B., Barros, D., Paulino, I., Essien, P., et
640 al.: Equatorial plasma bubble occurrence under propagation of MSTID and MLT gravity
641 waves. *J. Geophys. Res.: Space Physics*, 125, e2019JA027566.
642 <https://doi.org/10.1029/2019JA027566>, 2020.
643

644 Takahashi, H., Essien, P., Figueiredo, C. A. O. B., Wrasse, C. M., Barros, D., Abdu, M. A.,
645 Otsuka, Y., Shiokawa, K., and Li, G. Z.: Multi-instrument study of longitudinal wave
646 structures for plasma bubble seeding in the equatorial ionosphere. *Earth Planet. Phys.*, 5(5),
647 368–377. <https://doi.org/10.26464/epp2021047>, 2021.
648

649 Taori, A., Makela, J. J., and Taylor, M. J.: Mesospheric wave signatures and equatorial
650 plasma bubbles: A case study, *J. Geophys. Res.*, 115, A6, A06302,
651 <https://doi.org/10.1029/2009JA015088>, 2010.
652

653 Taori, A., Jayaraman, A., and Kamalakar, V.: Imaging of mesosphere–thermosphere airglow
654 emissions over Gadanki (13.5° N, 79.2° E): First results. *J. Atmos. Sol.-Terr. Phys.*, 93, 21-
655 28. <https://doi.org/10.1016/j.jastp.2012.11.007>, 2013.

656

657 Taori, A., Parihar, N., Ghodpage, R., Dashora, N., Sripathi, S., Kherani, E. A., and Patil, P. T.
658 (2015). Probing the possible trigger mechanisms of an equatorial plasma bubble event based
659 on multistation optical data. *J. Geophys. Res. Space Physics*, 120, 8835-8847.
660 <https://doi.org/10.1002/2015JA021541>.

661

662 Tsunoda, R. T.: On seeding equatorial spread F: Circular gravity waves, *Geophys. Res. Lett.*,
663 37, L10104, <https://doi.org/10.1029/2010GL043422>, 2010.

664

665 Tulasi Ram, S., Yamamoto, M., Tsunoda, R. T., Chau, H. D., Hoang, T. L., Dantie, B.,
666 Wassae, M., Yatini, C. Y., Manik, T., and Tsugawa, T.: Characteristics of large-scale wave
667 structure observed from African and Southeast Asian longitudinal sectors, *J. Geophys. Res.*
668 *Space Physics*, 119, 2288-2297, <https://doi.org/10.1002/2013JA019712>, 2014.

669

670 Vadas, S. L., and Azeem, I.: Concentric secondary gravity waves in the thermosphere and
671 ionosphere over the continental United States on 25-26 march 2015 from deep convection. *J.*
672 *Geophys. Res. Space Physics*, 126, e2020JA028275. <https://doi.org/10.1029/2020JA028275>,
673 2021.

674

675 Wrasse, C. M., Figueiredo, C. A. O. B., Barros, D., Takahashi, H., Carrasco, A. J., Vital, L.
676 F. R., Rezende, L. C. A., Egito, F., Rosa, G. M., and Sampaio, A. H. R.: Interaction between
677 Equatorial Plasma Bubbles and a Medium-Scale Traveling Ionospheric Disturbance,
678 observed by OI 630 nm airglow imaging at Bom Jesus de Lapa, Brazil. *Earth Planet. Phys.*,
679 5(5), 397–406. <https://doi.org/10.26464/epp2021045>, 2021.

680

681 Woodman, R. F.: Spread F: An old equatorial aeronomy problem finally resolved? *Ann.*
682 *Geophys.*, 27(5), 1915-1934. <https://doi.org/10.5194/angeo-27-1915-2009>, 2009.

683

684 Yadav, S., Sridharan, R., Sunda, S. and Pant, T. K.: Further refinements to the spatiotemporal
685 forecast model for L-band scintillation based on comparison with C/NOFS observations, *J.*
686 *Geophys. Res. Space Physics*, 122, 5643-5652, <https://doi.org/10.1002/2017JA023869>, 2017.

687

688 Zalesak, S., and Ossakow, S.: Nonlinear equatorial spread F: Spatially large bubbles resulting
689 from large horizontal scale initial perturbations. *J. Geophys. Res.*, 85(A5), 2131-2142.
690 <https://doi.org/10.1029/JA085iA05p02131>, 1980.

691

692 **Figure Captions**

693 **Figure 1.** ASAI images during 1742-1830 UT over Ranchi (23.3° N, 85.3° E, mlat. $\sim 19^\circ$ N)
694 on 16 April 2012. DP1 is the first fossil plasma depletion that showed GWs driven revival.
695 Depletions OD1 and OD2 preceded depletion DP1. ROI1 is the region-of-interest wherein the
696 south-north propagating GW activity and faint signatures of eastward drifting depletion DP1
697 were seen initially. Some weakly noticeable GWs fronts are 'f1', 'f2' and 'f3' (in
698 succession). 't1' and 't2' are trough that precede fronts 'f1' and 'f2', respectively. 'S1' and
699 'S2' are the fractions of fronts 'f1' and 'f2', respectively, that subsequently got linked to the
700 west wall of depletion DP1.

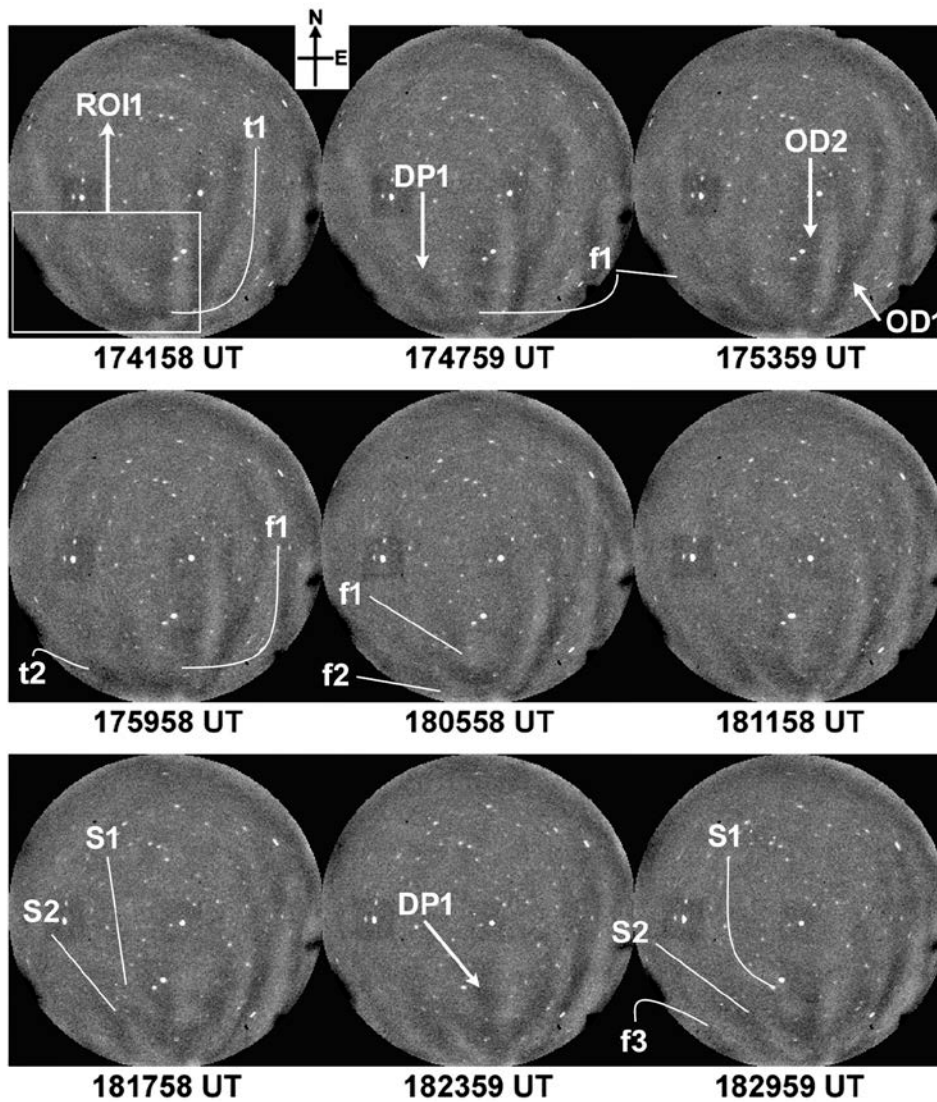
701
702 **Figure 2.** Same as Figure 1 but for 1836-1942 UT. DP2 is the second fossil depletion that
703 showed GWs driven revival. Some noticeable GWs fronts are 'f3' and 'f4'. A1 and A2 are
704 two arc-shaped regions of airglow enhancement near the east and west wall of depletion DP1.
705 ROI2 is the region-of-interest wherein ambient plasma diffusion occurred across the west
706 wall of depletions DP1.

707
708 **Figure 3.** Typical time difference ASAI of OI 630 nm emission over Ranchi showing GW
709 activity during 1742–1830 UT.

710
711 **Figure 4.** (a)-(b) North-south (NS) keogram along 84.4° E and 85.3° E longitude generated
712 from OI 630 nm images during 1730-1930 UT. Alternating bright and dark intensity
713 striations (i.e. wave traces) can be seen over North. Probably depletions masked GWs
714 features over South, and hence, these wave traces were not seen. Slope of these striations
715 indicates towards the south-north movement of GW fronts. A few clear wave traces that were
716 used to estimate speed of GWs are marked by black arrow as 'b1', 'b2', 'b3' and 'b4'.

717
718 **Figure 5.** (a) Scatter plot of the TEC along the track of IPPs for a few GPS satellites over
719 Hyderabad (17.3° N, 78.6° E, mlat. $\sim 12.0^\circ$ N) during 1630-1930 UT on 16 April 2012. PRN
720 numbers of GPS satellites along with the start time at 1700 UT are marked adjacent to the
721 corresponding IPPs trajectory. G28's trajectory lay close to the south-west sector of the
722 ASAI. Imager's field-of-view is shown by dashed quarter circle with its centre at Ranchi. (b)
723 TEC variations of a few satellites showing the presence of GWs activity.

724



725

726

727

728

729

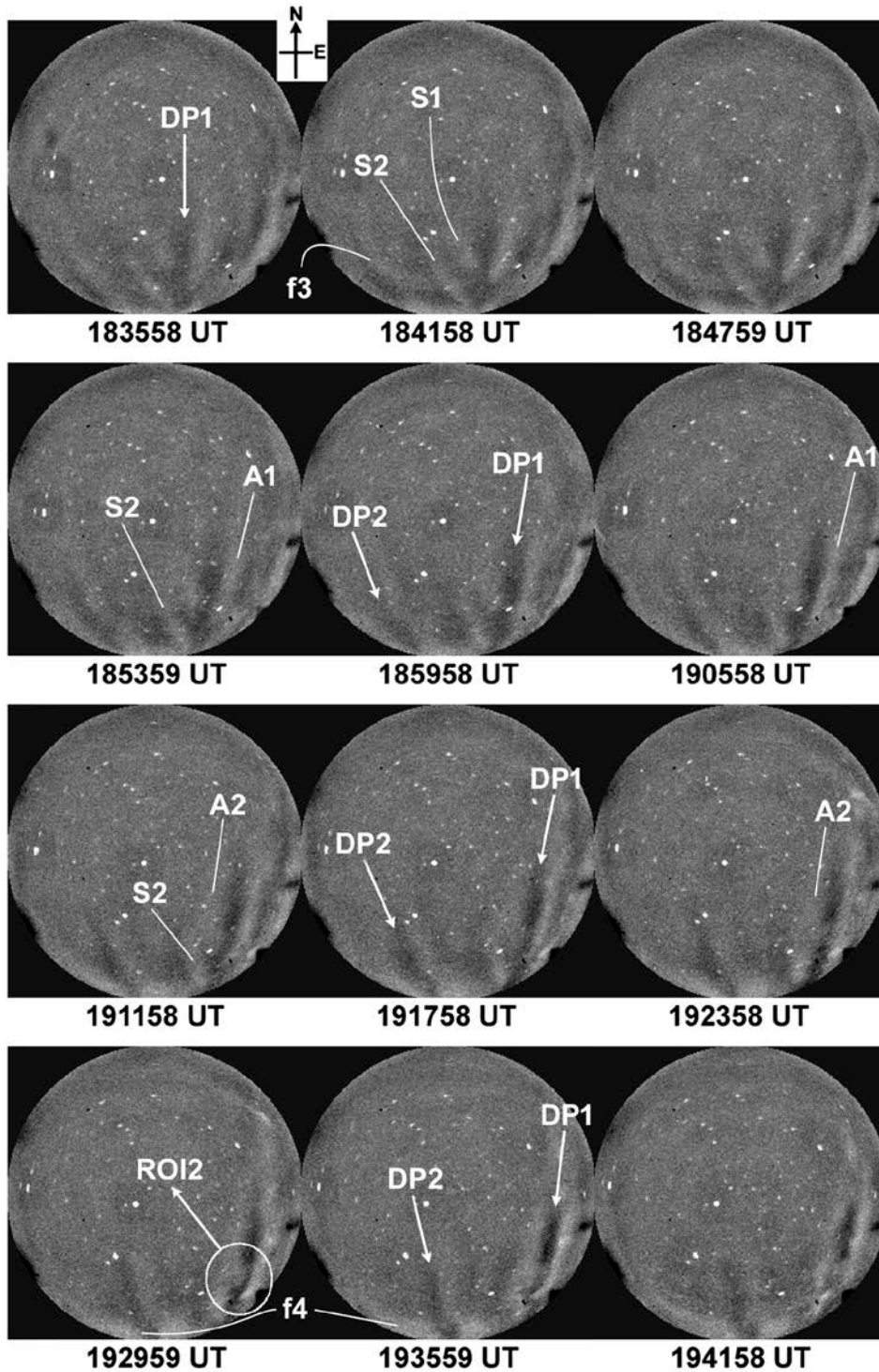
730

731

732

733

Figure 1. ASAI images during 1742-1830 UT over Ranchi (23.3° N, 85.3° E, mlat. ~19° N) on 16 April 2012. DP1 is the first fossil plasma depletion that showed GWs driven revival. Depletions OD1 and OD2 preceded depletion DP1. ROI1 is the region-of-interest wherein the south-north propagating GW activity and faint signatures of eastward drifting depletion DP1 were seen initially. Some weakly noticeable GWs fronts are 'f1', 'f2' and 'f3' (in succession). 't1' and 't2' are trough that precede fronts 'f1' and 'f2', respectively. 'S1' and 'S2' are the fractions of fronts 'f1' and 'f2', respectively, that subsequently got linked to the west wall of depletion DP1.



734

735

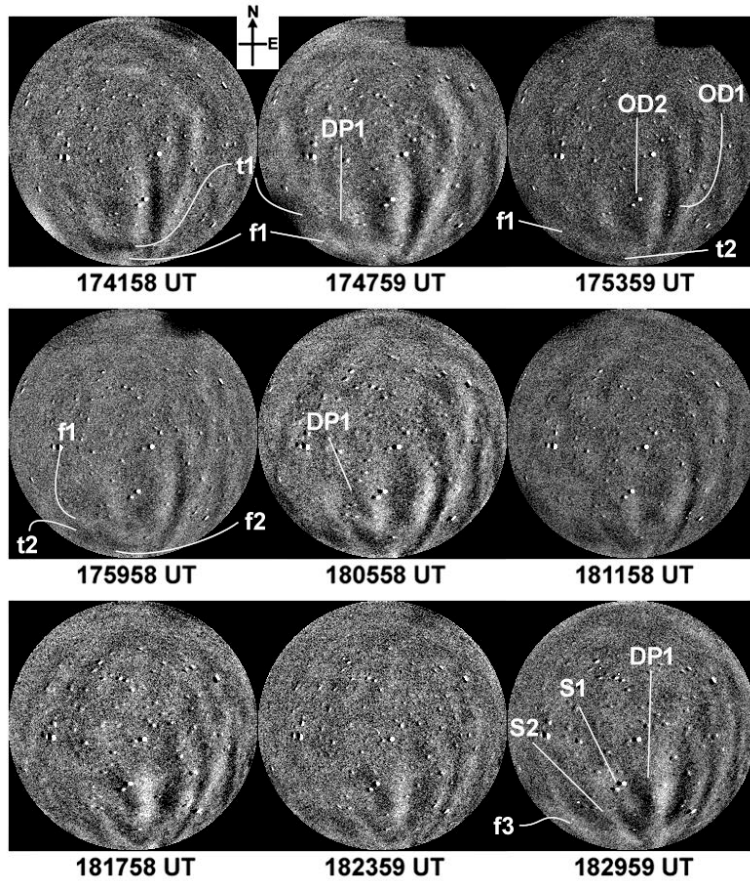
736

737

738

739

Figure 2. Same as Figure 1 but for 1836-1942 UT. DP2 is the second fossil depletion that showed GWs driven revival. Some noticeable GWs fronts are 'f3' and 'f4'. A1 and A2 are two arc-shaped regions of airglow enhancement near the east and west wall of depletion DP1. ROI2 is the region-of-interest wherein ambient plasma diffusion occurred across the west wall of depletions DP1.

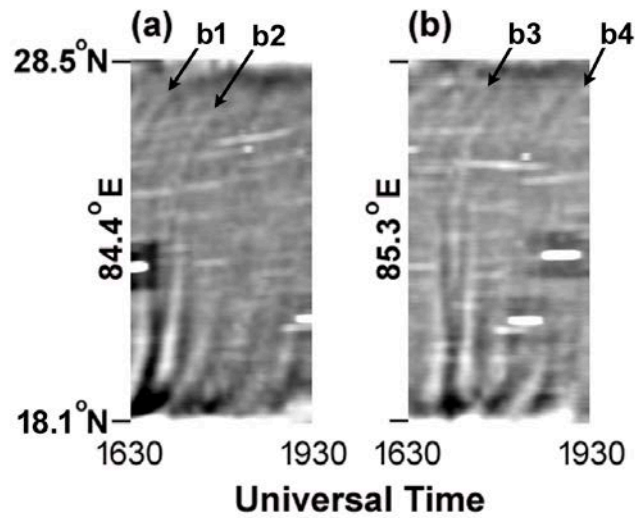


740

741

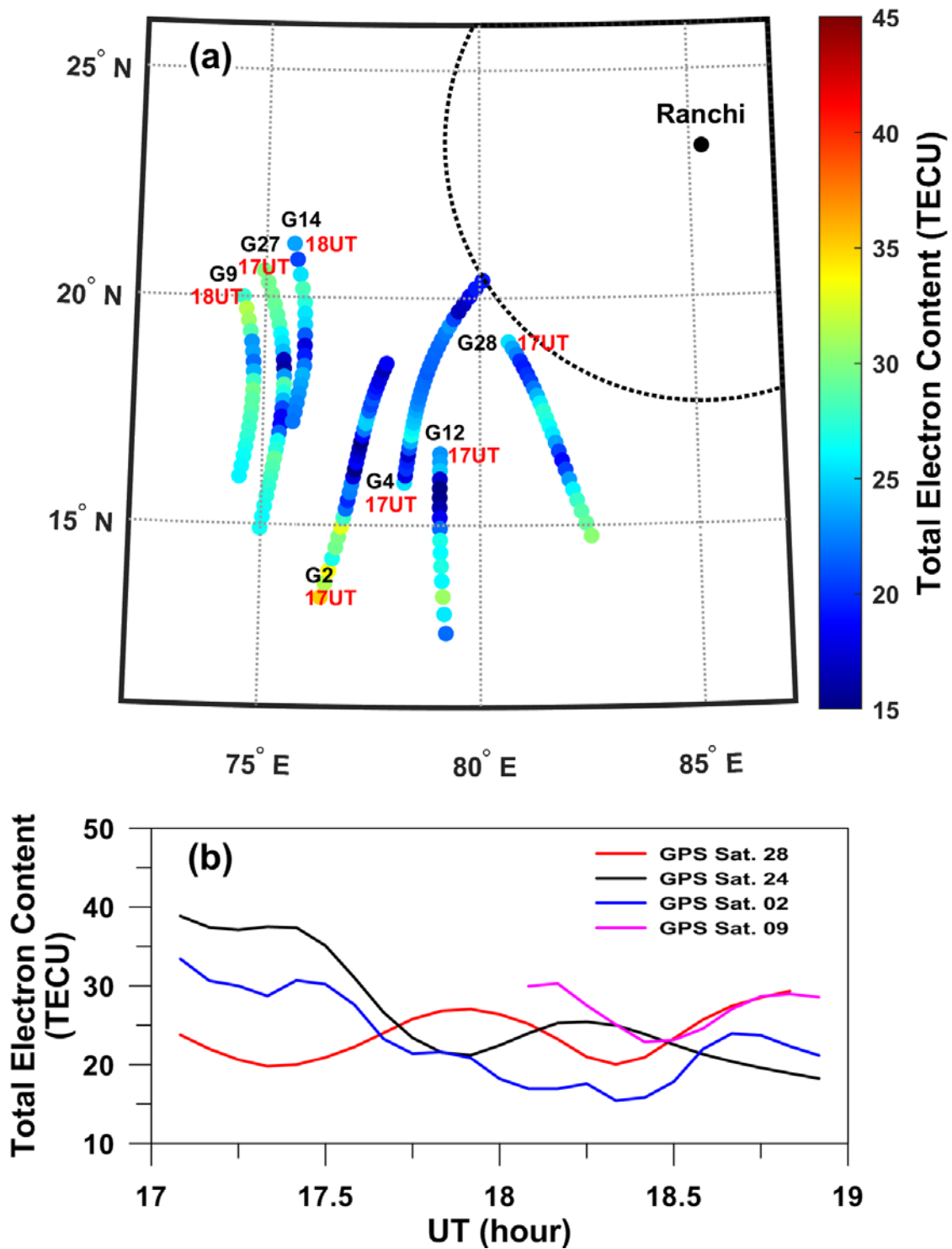
742

Figure 3. Typical time difference ASAI of OI 630 nm emission over Ranchi showing GW activity during 1742–1830 UT.



743
 744
 745
 746
 747
 748
 749
 750

Figure 4. (a)-(b) North-south (NS) keogram along 84.4° E and 85.3° E longitude generated from OI 630 nm images during 1730-1930 UT. Alternating bright and dark intensity striations (i.e. wave traces) can be seen over North. Probably depletions masked GWs features over South, and hence, these wave traces were not seen. Slope of these striations indicates towards the south-north movement of GW fronts. A few clear wave traces that were used to estimate speed of GWs are marked by black arrow as 'b1', 'b2', 'b3' and 'b4'.



751
 752
 753
 754
 755
 756
 757

Figure 5. (a) Scatter plot of the TEC along the track of IPPs for a few GPS satellites over Hyderabad (17.3° N, 78.6° E, mlat. ~12.0° N) during 1630-1930 UT on 16 April 2012. PRN numbers of GPS satellites along with the start time at 1700 UT are marked adjacent to the corresponding IPPs trajectory. G28's trajectory lay close to the south-west sector of the ASAI Imager's field-of-view is shown by dashed quarter circle with its centre at Ranchi. (b) TEC variations of a few satellites showing the presence of GWs activity.

758 **Supplementary Material**

759 **Supplementary Material S1:** Movie created from all-sky 630 nm nightglow images
760 showing the gravity wave activity and the evolution of depletion DP1 and DP2 (available
761 from <https://doi.org/10.5281/zenodo.8358134>).